Journal of Physics: Condensed Matter

PAPER • OPEN ACCESS

Magnetoelastic properties and behaviour of 4C pyrrhotite, Fe_7S_8, through the Besnus transition

To cite this article: C R S Haines *et al* 2020 *J. Phys.: Condens. Matter* **32** 405401

OPEN ACCESS
IOP Publishing
Journal of Physics: Condensed Matter
J. Phys.: Condens. Matter **32** (2020) 405401 (17pp)
https://doi.org/10.1088/1361-648X/ab8fd3

Magnetoelastic properties and behaviour of 4C pyrrhotite, Fe_7S_8, through the Besnus transition

C R S Haines[1,5], S E Dutton[2], M W R Volk[3,4] and M A Carpenter[1]

[1] Department of Earth Sciences, University of Cambridge, Downing Street, Cambridge CB2 3EQ, United Kingdom
[2] Cavendish Laboratory, University of Cambridge, Madingley Road, Cambridge CB3 0HE, United Kingdom
[3] Institute for Rock Magnetism, Department of Earth Sciences, University of Minnesota, 116 Church Street SE, Minneapolis, Minnesota 55455, United States of America
[4] Department of Earth and Planetary Science, Harvard, 24 Oxford Street, Cambridge, MA 02138, United States of America

E-mail: crsh2@cam.ac.uk

Received 27 February 2020, revised 20 April 2020
Accepted for publication 4 May 2020
Published 26 June 2020

Abstract

Pyrrhotite, Fe_7S_8, is a commonly occurring carrier of magnetic remanence and has a low temperature transition, the Besnus transition, involving a change in spin state. Variations of the thermodynamic, magnetic and elastic properties through this transition at ~33 K in a natural sample of 4C pyrrhotite have been tested against a group theoretical model for coupling between order parameters relating to Fe/vacancy ordering (irrep $U_1(1/2,0,1/4)$) and magnetic ordering (irreps $m\Gamma_4^+$ and $m\Gamma_5^+$). Magnetoelastic coupling is weak but the pre-existing microstructure of ferroelastic and magnetic domains, that develop as a consequence of Fe/vacancy and ferrimagnetic ordering during slow cooling in nature ($P6_3/mmc \rightarrow C2'/c'$), causes subtle changes in the low temperature transition ($C2'/c' \rightarrow P\bar{1}$). The Besnus transition involves a rotation of magnetic moments out of the a–c plane of the monoclinic structure, but it appears that the transition temperature might vary locally according to whether it is taking place within the pre-existing domain walls or in the domains that they separate. Evidence of metamagnetic transitions suggests that the magnetic field–temperature phase diagram will display some interesting diversity. Low temperature magnetic transitions in minerals of importance to the palaeomagnetism community have been used to identify the presence of magnetite and haematite in rocks and the Besnus transition is diagnostic of the existence of pyrrhotite, Fe_7S_8.

Keywords: pyrrhotite, magnetoelastic coupling, Besnus

Supplementary material for this article is available online

(Some figures may appear in colour only in the online journal)

[5] Author to whom any correspondence should be addressed.

1. Introduction

Minerals which hold a remanent magnetic signal for tens to hundreds of millions of years provide a material record against which models of the evolution of the Earth's magnetic field and past tectonic plate motions have been tested. Hematite (Fe_2O_3)–ilmenite ($FeTiO_3$) and magnetite (Fe_3O_4)–ülvospinel (Fe_2TiO_4) are the most important solid solutions in this context but have proved to be of intrinsic interest also for the phenomenological richness of the magnetic and structural instabilities which they display. In addition to the initial magnetisation which provides the palaeomagnetic record, hematite has a spin flop transition (the Morin transition) at ∼260 K [1], magnetite has a charge order transition (the Verwey transition) at ∼122 K [2, 3] which is also ferroelastic, hemo-ilmenite undergoes Fe/Ti ordering, and glassy magnetic behaviour occurs at low temperatures in Ti-rich members of the hematite–ilmenite solid solution [4]. In ülvospinel, the magnetic transition at ∼125 K is accompanied by cooperative Jahn–Teller distortions [5].

Although not quite as widely relevant from a geological perspective, the sulphide mineral pyrrhotite ($Fe_{1-x}S$) also has the potential to preserve a valuable palaeomagnetic signal [6–8], including for meteorites and the crust of Mars [9, 10]. However, it has an even more remarkable diversity of magnetic properties over a narrow composition range ($0 < x \leqslant 0.125$) due to the fact that small changes in iron content lead to a variety of superstructures associated with ordering of vacancies on the cation site [11–16]. There is a uniform Néel temperature of ∼590 K across the pyrrhotite solid solution, $Fe_{1-x}S$ with $0 < x \leqslant 0.125$, [12, 14] above which the structure is hexagonal with space group $P6_3/mmc$ (NiAs structure). When $x < 0.125$ the magnetic ordering is antiferromagnetic with moments confined to the hexagonal basal plane. The magnetic moments are on layers of iron atoms and are ferromagnetically aligned within the layer. Neighbouring layers are coupled antiferromagnetically. When $x = 0.125$ the vacancies occupy only one of the antiferromagnetic sublattices, leading to a bulk ferrimagnetic moment. When $0.08 < x \leqslant 0.125$ the iron vacancies order and it is this vacancy ordering that gives rise to the range of closely related superstructures. Two features in common across all these phases and their multiple instabilities are coupling between different order parameters and the development of spontaneous strain due to spin–lattice and spin–orbital effects. The primary objective of the present study was to investigate magnetoelastic and order parameter coupling associated with the low temperature transition at ∼35 K in a natural sample of pyrrhotite with composition Fe_7S_8. This transition has drawn comparisons with the Morin transition in hematite and the Verwey transition in magnetite [17–21], with a suggestion of influence due to the Jahn–Teller effect [22].

Rochette *et al* (2011) [18] suggested that the low temperature transition in crystals with composition close to Fe_7S_8 be named after Marie–Jeanne Besnus who, in 1964 [17], reported an anomaly in the resistivity and magnetisation at 30 K. She commented also that it was coincident with a broad feature in the heat capacity reported five years earlier by Grønvold *et al* [23]. The transition came to prominence in the literature after the associated drop in magnetic moment in natural crystals was reported by Fillion and Rochette [19] Dekkers *et al* [24] and Rochette *et al* [8]. It was also seen in Mössbauer spectra, which showed a splitting of one of the crystallographic sites into two equally populated subsites [22, 25]. Since then, the transition has been investigated in great detail using a variety of techniques, including x-ray diffraction [26], neutron diffraction [27–30] DC magnetometry [20, 31–38], AC magnetometry [21, 32, 36, 37], calorimetry [21, 23, 34], electrical resistivity [21, 34], Mössbauer spectroscopy [22, 25, 39], small angle neutron scattering [21], and torque magnetometry [40, 41]. Reported changes in temperature-dependence of the structural parameters, magnetic properties and electrical conductivity appear to be consistent with a discrete, thermodynamically continuous phase transition [21, 30, 32, 34, 36, 38, 40, 41]. A discrete reduction in symmetry is also suggested at an atomic scale by the Mössbauer evidence of splitting of one of the cation sites [22, 25].

The crystallographic space group of 4C pyrrhotite is $C2/c$ at room temperature. Magnetic moments are aligned perpendicular to the b-axis within a plane which is a few degrees from (001) [28]. With falling temperature, the moments rotate progressively towards the direction of the crystallographic c-axis within the a–c plane [27, 28, 30, 34]. Wolfers *et al* (2011) [29] proposed that the Besnus transition involves a symmetry change from $F2/d$ (a convenient non-standard setting of $C2/c$) to $P1$ or $P\bar{1}$. It has not yet been possible to detect any distortion from monoclinic lattice geometry [30], but the proposed change in space group is consistent with group theoretical considerations of how the magnetism couples with the vacancy ordering [42]. At a macroscopic scale there is a change to four-fold symmetry in the orientation of easy magnetic directions within the a–b plane [29, 38]. Koulialias *et al* [41] also reported the emergence of this four-fold symmetry in torque measurements, but they had previously considered changes in properties of their sample to be an extrinsic effect due to the presence of two epitaxially intergrown superstructures [34, 36].

Changes in lattice parameters accompanying the symmetry change $P6_3/mmc \rightarrow C2/c$ at 598 ± 5 K shown by Powell *et al* (2004) [28] arise by strain coupling with an order parameter for the 4C vacancy ordering scheme and an order parameter for the ferrimagnetic ordering [43]. Variations in lattice parameters below T_B are much smaller [30] but are sufficient to confirm that there is significant coupling of strain also with the second magnetic order parameter. It follows that there must be coupling between two magnetic order parameters and a vacancy/structural order parameter. Because the symmetry changes are hexagonal → monoclinic → triclinic, there will be some contribution to the overall pattern of strain relaxation from ferroelasticity and the resulting microstructures must contain some combination of interacting antiphase domains, magnetic domain walls and ferroelastic twin walls.

Here we present new heat capacity, magnetic, elastic and anelastic data collected as a function of temperature and magnetic field to show that the Besnus transition in a natural pyrrhotite crystal with composition Fe_7S_8 appears to occur in stages which depend on the orientation of the field with respect to different crystallographic twins arising from the hexagonal $\rightarrow$ 4C monoclinic transition. Static magnetic measurements as a function of temperature in three directions have revealed how the ferromagnetic moment evolves both above and below the transition temperature, T_B. The role of strain is considered in respect of the transition and microstructure dynamics through determinations of the temperature- and field-dependent variations of elastic constants and acoustic loss, measured by Resonant Ultrasound Spectroscopy (RUS). Magnetoelastic and order parameter coupling behaviour associated with the hexagonal ($P6_3/mmc$)–monoclinic ($C2'/c'$) transition in the same sample is described in a separate paper (Haines *et al* 2020a [43]).

2. Sample description

A natural 4C pyrrhotite sample with composition $Fe_{7.00(6)}S_8$ was obtained from the mineral collection of the South Australia Museum and has been described in detail by Haines *et al* (2019b) [43]. It had well developed crystal faces parallel to {001} and {100}, as defined with respect to hexagonal axes. Rectangular parallelepipeds, with faces cut perpendicular to [001], [100] and [$\bar{1}$20], were prepared from it using a fine annular saw. Crystal 1 had dimensions 1.279 × 1.325 × 1.735 mm^3 and mass 12.8 mg, and was used for measurements of heat capacity and AC magnetism. Crystal 2 (1.461 × 1.306 × 1.735 mm^3, 15.4 mg) was used for measurements of DC magnetisation. Crystal 3 (1.461 × 1.515 × 1.735 mm^3, 17.4 mg) was used for RUS at low temperatures. In each measurement involving an applied magnetic field, the orientation of the field was chosen to be perpendicular to one of the cut faces of the parallelepiped and is therefore specified below as being parallel to one of the (hexagonal) reciprocal lattice directions, [001]*, [100]* and [$\bar{1}$20]*.

It is inevitable that the parent crystal contained multiple magnetic domains from ferrimagnetic ordering and ferroelastic twins from the rhombohedral $\rightarrow$ monoclinic symmetry change associated with vacancy ordering. There are expected to be six possible directions for the ferrimagnetic moment in the monoclinic structure. If all six twin domains were present in equal proportions, the net moment would lie in the (001) plane without a unique direction. As set out below, values of the DC magnetic moments, $M_{[100]^*}$, $M_{[\bar{1}20]^*}$, $M_{[001]^*}$, measured in a field of 10 mT parallel to [100]*, [$\bar{1}$20]*, [001]* of crystal 2 gave the direction of the net moment, M, at room temperature as lying within (001), ∼54° away from [100]* and ∼36° away from [$\bar{1}$20]*. This falls close to the direction of the magnetisation which would represent the average, predominantly, of one pair of twin domains. Crystals 1 and 3 need not have had identical domain configurations but both will have had a net moment either within or very close to the (001) plane at room temperature.

3. Experimental

3.1. Heat capacity

Heat capacity measurements were carried out with and without an applied magnetic field in a quantum design PPMS. Crystal 1 (12.8 mg) was held on the puck with Apiezon N grease. Two sets of data were collected over the same temperature range for each setting of the external magnetic field. The first was of the puck plus grease, to give the background heat capacity. The second was of the puck, grease and crystal, from which the measured background was subtracted in order to retrieve the heat capacity of the crystal. In all cases the sample was cooled in zero field. At low temperatures the heat capacity of the crystal was large compared with the background. At temperatures above ∼30 K the background heat capacity was larger than that of the crystal.

3.2. DC magnetism

Magnetisation was measured using a Quantum Design MPMS. Crystal 2 (15.4 mg) was held between two identical quartz cylinders inside a brass half tube with [001]*, [100]* or [$\bar{1}$20]* aligned parallel to the magnetic field. Zero-field cooled (ZFC) data were collected by cooling the crystal to 2 K in zero applied field before measuring the moment in a field of 10 mT while heating back up to 300 K. Field cooled (FC) data were collected by first cooling the crystal from room temperature in a 5 T field. The field was switched off at 2 K and the magnetisation then measured in a 10 mT field during heating. Temperature was stabilised at each setpoint during measurements with H//[001]* direction and swept continuously at 3 K min^{-1} during measurements with H//[100]* or [$\bar{1}$20]* directions. Hysteresis loops were subsequently measured in the three principal directions at a selection of temperatures in fields between +5 and -5 T. In between measurements of the hysteresis at different temperatures the sample was heated well above the Besnus transition temperature and cooled to the target temperature in zero field.

3.3. AC magnetism

AC magnetic measurements were carried out on crystal 1 (12.8 mg) using the ACMS II option of a Quantum Design PPMS, with a DC field of 2 mT and an AC field of 0.3 mT at frequencies of 0.01, 0.1, 1 and 10 kHz. Measurements were made on heating after cooling in zero field.

3.4. Resonant Ultrasound Spectroscopy

The RUS technique has been described in detail in the literature [44–48]. It involves excitation of acoustic resonances of a mm-sized sample and measurement of the frequency, f, and peak width at half height, Δf, of peaks in the resulting spectrum. Resonant modes are dominated by shearing motions so that the results from individual peaks provide information predominantly relating to shear elastic constants. Values of the elastic constants of the sample scale with f^2. Acoustic loss is

expressed in terms of the inverse mechanical quality factor, Q^{-1}, which is usually taken to be $\Delta f/f$.

For the low temperature experiments described here, crystal 3 (17.4 mg) was placed across a pair of faces between the two transducers in a holder that has been described by McKnight *et al* (2007) [49]. The holder was lowered into an Oxford Instruments Teslatron cryostat which has a superconducting magnet capable of delivering a magnetic field of up to 14 T [50, 51]. Data were collected in automated sequences with varying temperature at constant field or with varying field at constant temperature. A settle time, generally of 10 min, was allowed for equilibration at each set point of temperature or 1 min at each set point of field. The orientation of the crystal was such that the magnetic field was applied parallel to $[\bar{1}20]^*$. We note here that due to the distance between the sample and the thermometer there is sometimes an offset between the measured and true sample temperature. The offset has been measured and is up to ~2 K in the region of 35 K where the Besnus transition is observed. We therefore rely on the heat capacity measurments to provide the most accurate estimate of the Besnus transition temperature.

4. Results

4.1. Heat capacity

Results of the temperature- and field-dependent heat capacity measurements through T_B are given in figure 1(a). Features at ~215 K and ~280 K seen in the insert, which shows data over the full temperature interval in zero field, are known to be artefacts. Apart from a slight shoulder at the high temperature side, the peak at 33 K in zero field looks like the classic excess heat capacity associated with a magnetic phase transition. There is a split into three overlapping peaks separated by ~1 K in data collected with a field applied parallel to $[100]^*$. The three peaks are best seen in the data collected in an applied field of 1 T (figure 1(a)). Each of these peaks shifts to higher temperatures with increasing field strength and their amplitudes also change systematically.

In order to determine the excess heat capacity, ΔC_p, and excess entropy, ΔS $(=\int \frac{C_p}{T}.\mathrm{d}T)$, associated with the structural/magnetic changes which occur below $T_B \approx 33$ K, it is necessary to generate a baseline for the high temperature reference state. Instead of following the conventional approach of fitting a polynomial function to the data above the transition point and extrapolating to lower temperatures, we have fitted a 5th order polynomial to the anomaly-free heat capacity between 2 K and 60 K of a sample of 5C pyrrhotite which had been produced by annealing a piece of the 4C starting crystal at 600 °C (see Haines *et al* 2020b [52]). The fit parameters were used to construct the baseline shown in the upper insert of figure 1(b). The resulting variations of ΔS, after integration of the differences, are shown in the main field of figure 1(b) (see appendix A1 for further details). Variations of ΔS with temperature extracted in this way yielded a total entropy change of ~−9 J mol^{-1} K and a tail above the transition point. The main differences between results obtained under

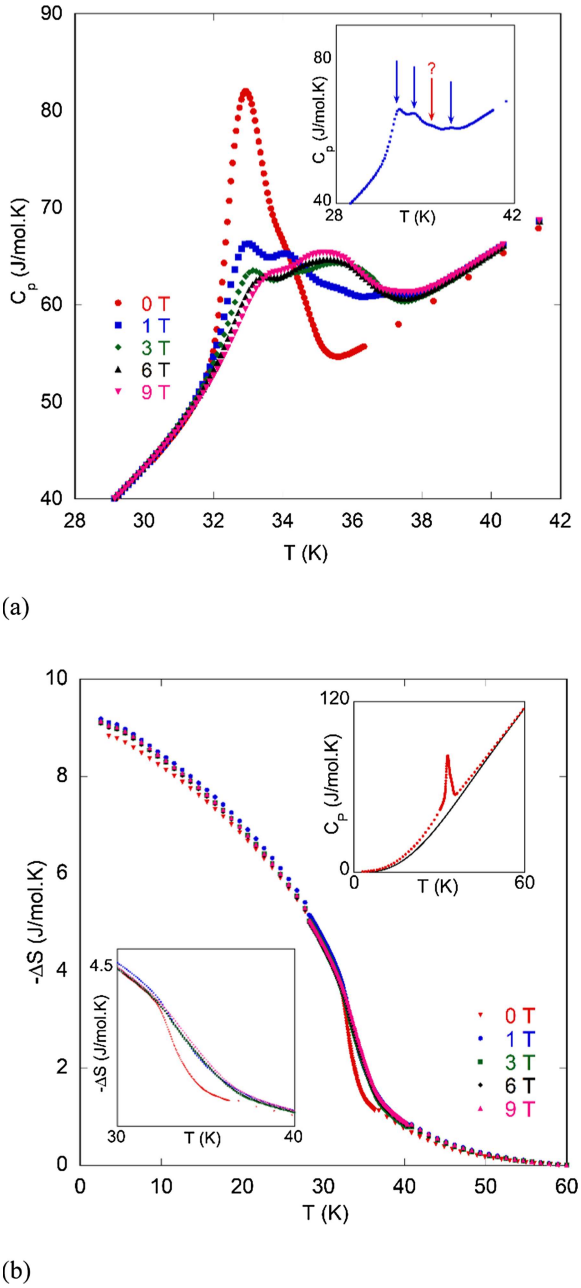

Figure 1. (a) Heat capacity anomaly associated with the Besnus transition, measured in zero field and with different magnetic field strengths applied parallel to $[100]^*$ of crystal 1. The zero field data show a strong peak at ~33 K and a slight shoulder at ~34 K. With increasing applied field, three overlapping peaks separated by ~1 K develop in systematically changing proportions and their maxima shift to slightly higher temperatures. The inset shows the data taken in an applied field of 1 T, showing the multiple peaks more clearly. Blue arrows show the positions of three distinct peaks while the red arrow and question mark show the position of a weaker feature. (b) Excess entropy, ΔS, due to the Besnus transition. The main effect of the applied field is to increase by ~3 K the temperature range over which the entropy changes through the transition point (lower insert).

different strengths of field applied parallel to $[100]^*$ occur in an interval of ~3 K through the transition point itself (lower insert of figure 1(b)). Heat capacity data for the same sample with the field applied perpendicular to the (001) plane show a

single peak pushed to higher temperature and broadened by the applied field (appendix A2).

4.2. DC magnetisation

Values of the magnetisation measured in a 10 mT field along $[100]^*$, $[\bar{1}20]^*$ and $[001]^*$ directions under FC and ZFC conditions are given as $M_{[100]^*}$, $M_{[\bar{1}20]^*}$ and $M_{[001]^*}$ in figure 2(a). There are small differences between FC and ZFC values in the interval ~35–300 K, steep changes in trend at the Besnus transition and large differences between FC and ZFC values below the transition point. Above T_B, the individual trends with falling temperature are of continuously decreasing magnetisation along $[100]^*$ and $[\bar{1}20]^*$ accompanied by a correlated increase along $[001]^*$. The net magnetisation, $M = \sqrt{M^2_{[100]*} + M^2_{[\bar{1}20]^*} + M^2_{[001]*}}$, decreases slightly at first and then more steeply below ~200 K (figure 2(b)). Variations in the orientation of M with temperature, as reconstructed from the three sets of measurements, are shown in terms of spherical coordinates in figure 2(b), where θ is the angle from Z and φ is the angle between X and the projection of the moment onto the XY plane. Tilting out of the (001) plane towards $[001]^*$ progressed to $\theta \sim 56^\circ$ at 35 K, in comparison with previously reported values of ~61° at 11 K (Powell *et al* 2004) [28] and ~66° at 35 K (Koulialias *et al* 2018c) [30] from neutron powder diffraction. Below T_B the direction of M rotates out of this plane, as found previously by Koulialias *et al* (2018c) [30]. The rotation observed here was from $\varphi \approx 60^\circ$ at 35 K to $\varphi \approx 90^\circ$ at 2 K (figure 2(b)). The value of the net magnetisation, $|M|$, first decreased by ~20 % between ~35 and ~30 K and then increased slightly down to 2 K (figure 2(b)). The maximum in $d|M|/dT$ occurs between ~31 and ~33 K (figure 2(c)).

It is important to realise that in the temperature interval between the Besnus transition and room temperature the system is in its fully ordered magnetic ground state with respect to the 595 K transition. The crystallographic twins are set, the vacancies will not reorder and the magnetic domains will be determined (in the absence of an applied field) by the sample geometry and microstructural details, including twinning. The applied measuring field is significant when compared to the coercive field ($H_c \sim 5$–10 mT [8, 32, 36]), and the moment measured is therefore an appreciable fraction of the saturation moment.

Cooling in a 5 T field resulted in significant changes in magnetisation in all three measuring directions below T_B (figure 2(a)). At 2 K $M_{[001]*}$ was greater than the ZFC value by a factor of ~3. Values of $M_{[100]^*}$ and $M_{[\bar{1}20]^*}$ from FC measurements were lower at 2 K than at 35 K. Clearly, a 5 T field applied parallel to $[001]^*$ is sufficient to cause a persistent poling of the low temperature structure, but if any poling occurred to give increased moments parallel to $M_{[100]^*}$ or $M_{[\bar{1}20]^*}$ it must have been lost when the field was switched off. During heating from 2 K, FC values of $M_{[001]^*}$ and $M_{[\bar{1}20]^*}$ returned to approximately ZFC values above ~35 K. The FC value of $M_{[100]^*}$ is persistently above the ZFC values from 2 to 31 K.

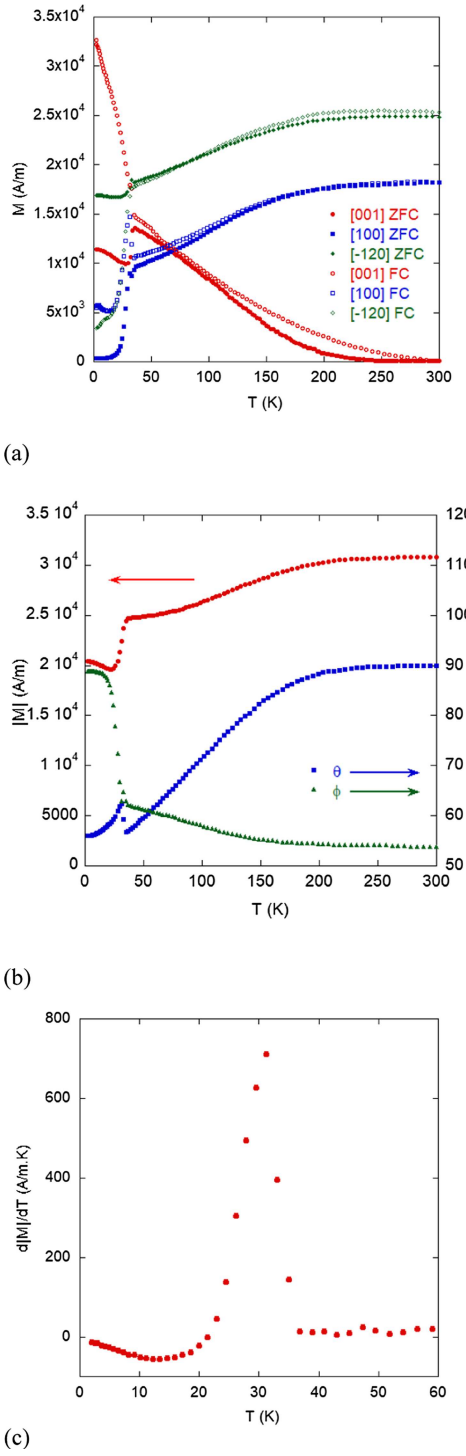

Figure 2. DC magnetic results for crystal 2. (a) FC (5 T field applied during cooling) and ZFC magnetisation data for three orthogonal directions in the crystal, as measured during heating in a 10 mT field. (b) Magnitude of the net magnetic moment, $|M|$ (left axis) and changes in orientation of the moment expressed in terms of spherical coordinates (right axis) calculated from the ZFC data. Blue squares show the temperature evolution of θ, the angle of the magnetisation vector from the c* axis, and green triangles the evolution of φ, the angle within the basal plane from the X-axis (the [001] direction of the parent NiAs structure). (c) $d|M|/dT^{-1}$ for net moment calculated from the ZFC data has a single peak at 31 K ± 1 K.

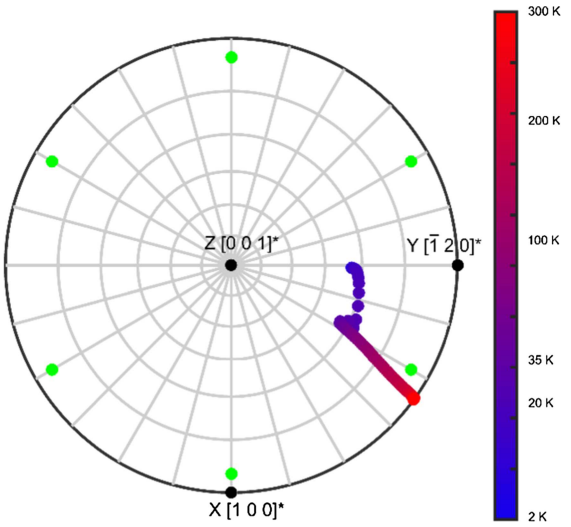

Figure 3. Orientation of the net ferrimagnetic moment, with respect to orthogonal reference axes, *X*, *Y* and *Z*. Directions of moments in the six possible twin domains of the monoclinic structure at room temperature, based on the structure of Powell *et al* (2004) [28], are shown as green circles. A red circle marks the orientation of the net magnetisation, *M*, in crystal 2 at room temperature, based on measurements made parallel to the three directions $[100]^*$, $[\bar{1}20]^*$ and $[001]^*$. Some combination of twins was inevitably present but the proximity of the measured direction of *M* to a green circle indicates which of these was predominant. Symbols with colours varying from red to blue show the trajectory of *M* with falling temperature, from analysis of ZFC data. The colour shows the temperature of the measurements. The decrease of red and increase of blue are both proportional to the square root of the temperature. This form of scaling was found to be the most effective at demonstrating the temperature dependence. Selected temperatures are labelled on the colour bar.

At this point there is a peak in the FC value of $M_{[100]*}$ and it then returns to the ZFC values over the interval 31 K to 35 K. Coercivities reported in the literature for temperatures above T_B are only ∼5–10 mT [8, 32, 36]. It is therefore not surprising that any poling of magnetic domains might not persist in a measuring field of 10 mT during heating to above ∼35 K in the FC sequence, though there are slight differences between FC and ZFC results up to 300 K.

Variations of the orientation of the net moment, *M*, from the ZFC measurements between 2 and 300 K are shown with respect to an orthogonal set of reference axes, *X*, Y and *Z*, in figure 3. In this setting $[100]^*$ of the hexagonal and monoclinic structures has been set parallel to *X*. $[\bar{1}20]^*$ of the hexagonal structure has been set parallel to Y, and is also parallel to [010] of the monoclinic structure. $[001]^*$ of the hexagonal structure is parallel to *Z*. $[001]^*$ of the monoclinic structure is not shown but $\beta \approx 90.5°$ at 300 K in space group setting *F*2/*d* (Powell *et al* 2004 [28]), and so is within ∼1° of $[001]^*$ of the hexagonal structure. Miller indices refer only to the hexagonal structure. The initial orientation was within the XY plane at an angle of ∼56° from *X* ($[100]^*$) and 34° from *Y* ($[\bar{1}20]^*$). This is shown as a red circle in figure 3 and is close to the orientation expected for one pair of the six possible twins. If only one twin was present, the moment would rotate towards *Z* along a straight line with $\varphi = 60°$ as temperature reduces from room temperature to ∼35 K. Below T_B, the orientation of *M* rotates out of this plane at approximately constant θ, ending up on the plane between *Y* and *Z* ($\varphi = 90°$) at 2 K.

Figure 4 contains hysteresis (*M*–*H*) loops measured in the three principal directions at a selection of different temperatures in fields up to ±5 T. They are similar in form to what has previously been shown in the literature (e.g. refs. [31, 32, 34, 38]). There is very little difference, if any, between the curves for $H//[100]^*$ and $H//[\bar{1}20]^*$ at 5 K (figure 4(a)). Both have narrow loops with a saturating magnetisation of approximately 2.5 μ_B. The remanent magnetisation, M_r, is ∼2.3 μ_B per formula unit and the coercive field, H_c, is ∼50 mT. M_r was ∼ 0.75 μ_B/f.u and H_c ∼ 170 mT for $H//[001]^*$, and the value of the moment at the field where the loop closed was lower than in the other two directions. $M_{[001]^*}$ has a linear dependence on applied field above 2 T and, by extrapolation, would only reach the saturation value of ∼2.5 μ_B at 14.8 T (figure 4(a) inset). The *M*–*H* loops were open at 5 and 20 K for all three measuring directions (figures 4(b)–(d) but the openings became too narrow to be resolved at all temperatures above T_B.

An additional anomaly is evident in the *M*–*H* data collected with $H//[\bar{1}20]^*$. At 40, 50 and 60 K there is a distinct break in slope at ∼0.6–0.7 T (figure 4(c)). A break in slope is evident at ∼0.5 T also in the measurements made at 100 K, but the effect is weaker. A similar feature has been seen before and was attributed to the presence of 4C and 5C structures [36]. The crystal used in the present study only contained the 4C phase, however, and the breaks in trend are more likely to have been due to a metamagnetic transition.

Data for $H//[001]^*$ collected at 5, 20, 40 and 60 K have the same pattern of variations as for the other orientations, ie open loops below T_B and very slightly open loops above T_B (figure 4(d)). However, the moment induced at 300 K was substantially less than at lower temperatures and in comparison with the other two directions. The insert in figure 4(d) shows that saturation was not reached even at 5 T, consistent with $[001]^*$ being a magnetically hard direction at room temperature [53].

4.3. AC magnetism

The variations of real, χ', and imaginary, χ'', components of magnetic susceptibility shown in figure 5 from the present study are closely similar to the AC magnetic response of other single crystal [21, 36] and powdered samples [32]. Variations of χ' and χ'' measured at 10 kHz through the temperature interval 20–55 K are shown for $H//[\bar{1}20]^*$ in figure 5(a) and for $H//[001]^*$ in figure 5(b). Data collected at 0.1, 1 and 1 kHz were qualitatively the same and, in particular, the temperature at which the peak in χ'' occurred did not change with frequency. The main features of the temperature dependence of χ'' are an increase as the transition was approached from above, a peak at ∼37 K, followed by a steep drop to more or less constant values below ∼35 K. These were accompanied by rounding of χ' as a precursor effect ahead of T_B, followed by a steep drop to very low values at ∼35 K. There is an additional small peak at ∼33 K in the data for

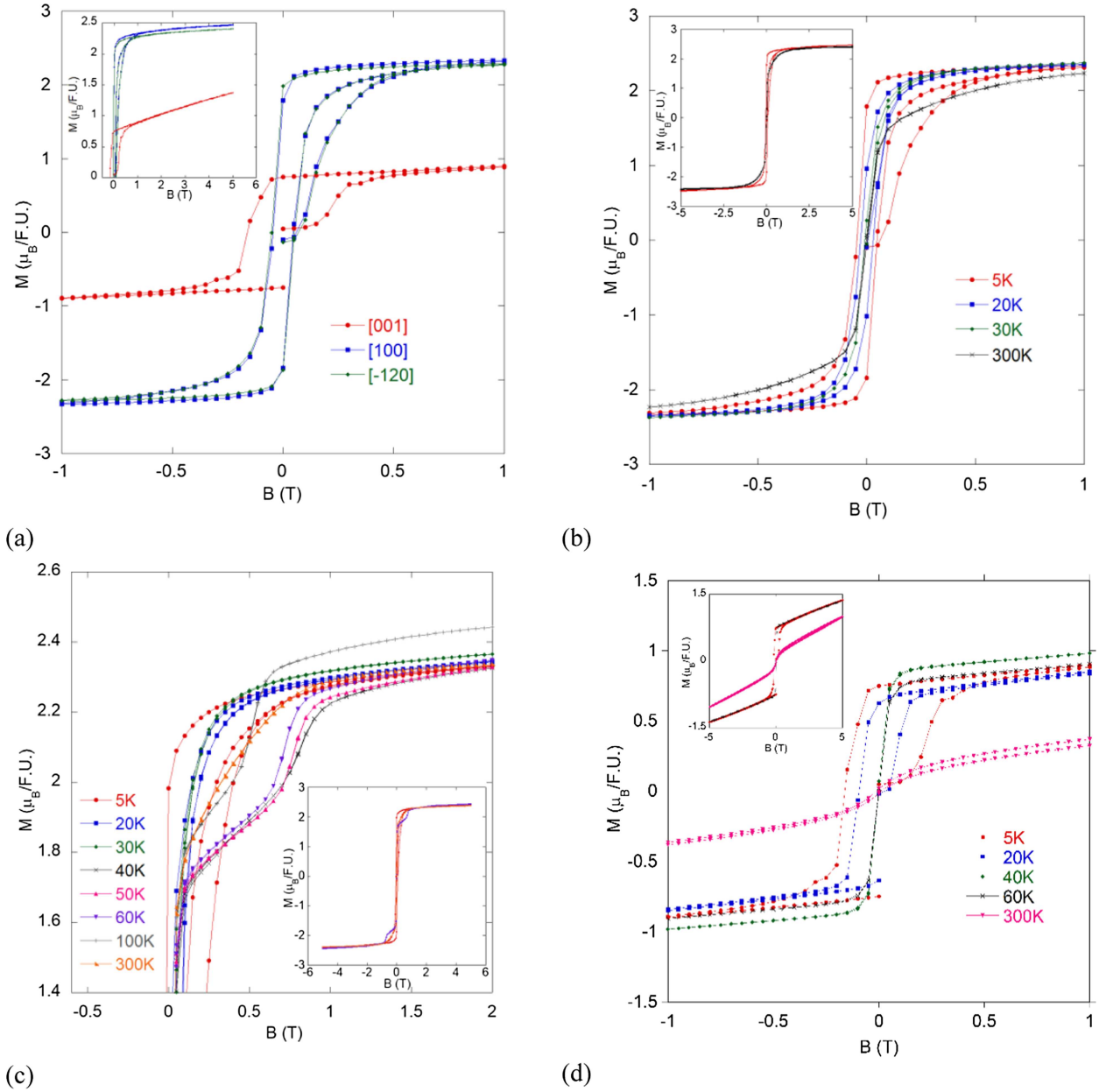

Figure 4. Magnetic hysteresis loops for crystal 2. (a) All three field directions at 5 K. (b) H//[100]* at different temperatures. Overtly open loops are seen only below T_B. (c) H//[$\bar{1}$20]*. Open loops are present at 5 and 20 K but are nearly closed at higher temperatures. There is evidence of a metamagnetic transition at 40 K and above, in the form of a distinct break in slope at fields of ∼0.6–0.7 T (40, 50, 60 K) and ∼0.5 T (100 K). (d) H//[001]*. Open loops are seen at 5 and 20 K. At 300 K the magnetisation in high fields is ∼50% lower than at $T \leqslant 60$ K.

H//[$\bar{1}$20]* (figure 5(a)) which is not present in the data for H//[001]* (figure 5(b)).

4.4. RUS

RUS spectra collected in a heating sequence from 5 K to 295 K are shown as a stack in figure 6(a). There are small increases and decreases in frequency of different resonance peaks showing that the single crystal elastic constants varied in a smooth but somewhat irregular manner through the temperature interval ∼150–295 K. More significant anomalies occurred near 35 K and the similarity of the trends for all the resonance peaks (figure 6(b)) indicates that the shear elastic constants followed closely similar patterns of softening/stiffening through the Besnus transition. Broadening of the peaks also indicates significant attenuation in the vicinity of T_B.

Variations of f^2 and Q^{-1} from fitting of representative resonance peaks collected in zero field are shown in figure 7(a) for the full temperature range and in figure 7(b) for small steps through T_B (see the supplemental material for results of analysis on multiple peaks, available online at http://stacks.iop.org/JPhysCM/32/405401/mmedia). The Besnus transition is marked by steep softening from either side, with an eventual increase in stiffness by ∼2–6 % below

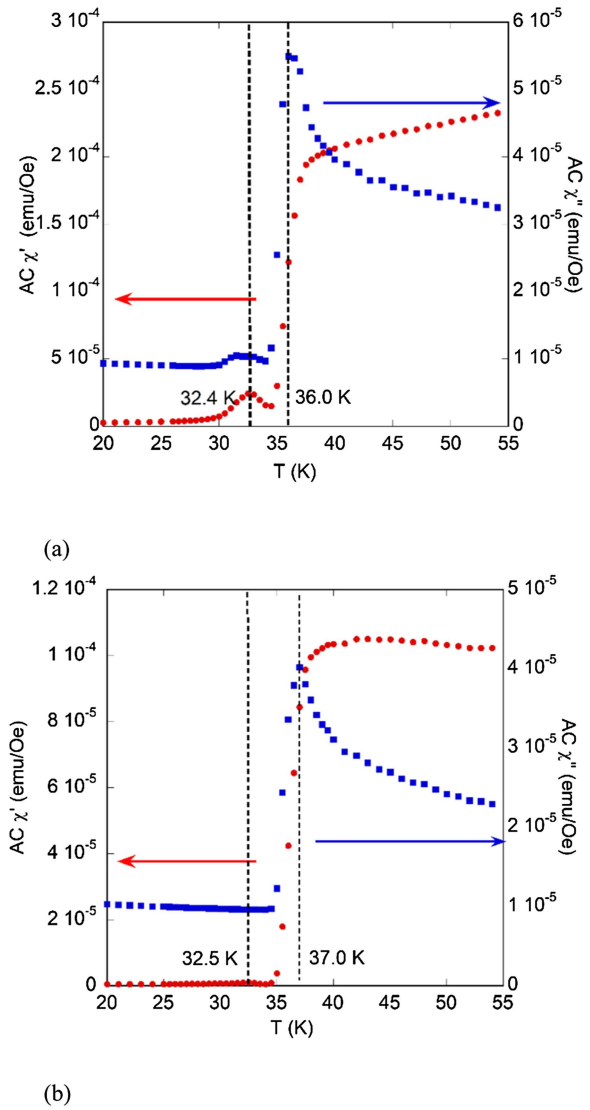

Figure 5. Variations of $\chi\prime$ (closed red circles) and $\chi\prime\prime$ (open blue squares) measured at 10 kHz through the Besnus transition. Crystal 1. (a) H//[$\bar{1}$20]*. (b) H//[001]*. Vertical dashed lines are a guide to the eye for the positions of the peaks.

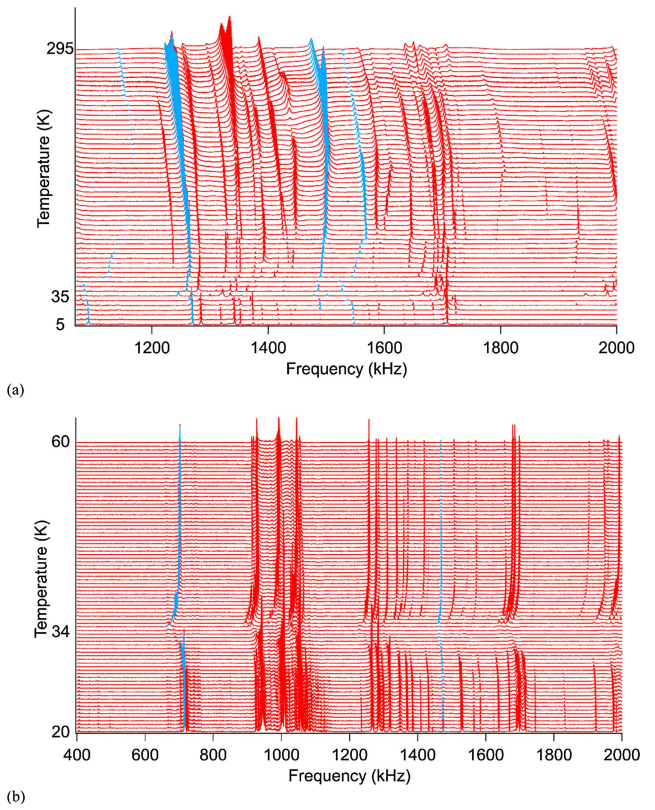

Figure 6. Primary RUS spectra from crystal 3, offset up the y-axis in proportion to the temperatures at which they were collected during heating. Blue curves are fits to selected resonance peaks, as used to extract variations in f^2 and Q^{-1}. (a) Spectra collected between 5 and 295 K show different patterns of smooth variations in the temperature interval ∼150–295 K, and a significant anomaly at ∼35 K. (b) Close-in view of spectra collected at 0.5 K intervals through the Besnus transition: the top spectrum was collected at 60 K and the bottom one at 20 K. Line broadening is indicative of acoustic attenuation in the vicinity of T_B.

the transition. The transition is also accompanied by marked increases in attenuation, with the maximum value of Q^{-1} occurring at ∼32 K (figure 7(b)). Above T_B there is hysteresis in the values of f^2 of some resonances between heating and cooling (figure 7(a)). These differences and the fact that the crystal ended up elastically softer by up to ∼6% are most likely due to a change in the proportions of different twin orientations following cycling through the Besnus transition. There is also an overall upward drift in the values of Q^{-1} with increasing temperature above T_B. Repeating the RUS measurements in fields of 2 T (figure 7(c)) and 9 T (figure 7(d)), applied parallel to [$\bar{1}$20]*, caused the temperature of the minimum in f^2 to shift upwards in temperature. The width of the minimum also broadened (figure 7(c)) and became two clearly resolved minima (figure 7(d)), apparently corresponding to two discrete phase transitions at ∼34.5 and ∼37.5 K.

Variations of f^2 and Q^{-1} for representative resonance peaks from spectra collected while increasing and decreasing the applied field parallel to [$\bar{1}$20]* at constant temperature are shown in figure 8 (see the supplemental material for results of analysis on multiple peaks). In the data for 60 K (figure 8(a)), a steep minimum in f^2 and a narrow peak in Q^{-1} imply that a metamagnetic transition occurred at ∼0.9 T. With increasing field, Q^{-1} initially decreased from its value at zero field and f^2 values were higher after the transition than they were before. This pattern was similar at 40 K (figure 8(b)), though the field at which the minimum in f^2 occurred is at ∼1.2 T. The pattern is completely different in data from the field sweep at 20 K, ie below T_B. With increasing field, there was a steep reduction in f^2 at ∼2 T, but there was then no recovery at higher fields. This was reversed when the field was reduced, but with a shift of the anomaly to ∼1.3 T. The loci of these anomalies were not explored for the other orientations of field but are consistent with the evidence from M–H data collected from crystal 2 that a metamagnetic transition occurred at ∼0.9 T when a field was applied parallel to [$\bar{1}$20]* at 40 and 60 K (figure 4(c)). On the other hand, the M–H loop measured at 20 K does not show evidence of metamagnetic transition. The anomaly in f^2 evident at 20 K might,

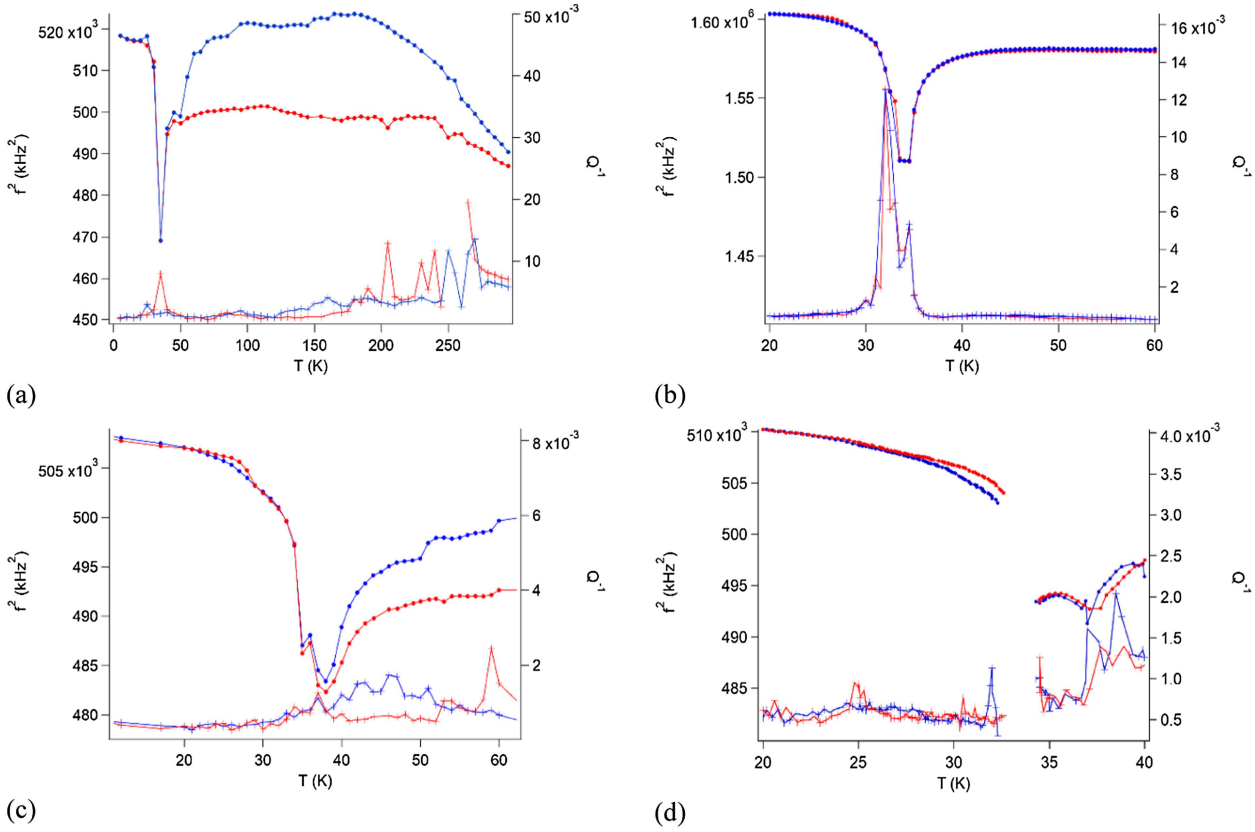

Figure 7. Temperature dependence of f^2 and Q^{-1} from fitting of representative peaks in RUS spectra from crystal 3. Blue = cooling, red = heating. (a) Zero field data for a resonance peak with $f \sim 700$ kHz at room temperature. The Besnus transition is marked by a steep minimum in f^2 and a peak in Q^{-1} at 34 K. f^2 ended up ∼6% lower on reheating above the transition than it had been during cooling. (b) Zero field data for a resonance peak with $f \sim 1220$ kHz at room temperature. The variation of Q^{-1} accompanying the minimum in f^2 at 34 K is resolved into two peaks, at 33 and 35 K. (c) Resonance peak with $f \sim 700$ kHz at room temperature, from spectra collected in a 2 T field applied parallel to $[\bar{1}20]^*$. The decrease in f^2 is over a wider temperature interval than seen for zero field and is shifted by up to 3 K. (d) Resonance peak with $f \sim 700$ kHz at room temperature, from spectra collected in a 9 T field applied parallel to $[\bar{1}20]^*$.

therefore, be related only to a change in the configuration of ferroelastic twin domains/ferrimagnetic domain walls.

RUS measurements were also undertaken on a separate sample characterised in the earlier work of Volk *et al* (2016) [38] and Volk *et al* (2018) [21]. The pattern of elastic softening was closely similar to that shown above and the minimum in f^2 occurred at 33 ± 1 K, consistent with the value of T_B estimated from other measurements such as heat capacity and resistivity [21, 38] (appendix A3). Small differences in the value of T_B between samples is likely to reflect differences in stoichiometry. The composition of the natural pyrrhotite sample used by Volk *et al* (2016) [38] and Volk *et al* (2018) [21] was $Fe_{7.2}S_8$.

5. Discussion

5.1. Order parameters and symmetry

Anomalies in heat capacity, magnetism and elasticity data through the temperature interval ∼30–35 K presented here for a natural sample of pyrrhotite with composition close to Fe_7S_8 are consistent with a discrete phase transition. This fits with a more general symmetry analysis in which different combinations of order parameters were considered to account for the vacancy and magnetic ordering transitions that have been identified in the $Fe_{1-x}S$ solid solution (Haines *et al* 2019 [42]). Space groups for the proposed sequence of structures with falling temperature in Fe_7S_8 were $P6_3/mmc$–$C2'/c'$–$P\bar{1}$, in agreement with the possibility of P1 or $P\bar{1}$ proposed by Wolfers *et al* (2011) [29] for the low temperature structure. The key order parameters and their non-zero components for this sequence were listed by Haines *et al* (2019a) [42]. The $P6_3/mmc \rightarrow C2'/c'$ transition is driven by a combination of vacancy ordering, for which the order parameter has the symmetry of $U_1(1/2,0,1/4)$, and magnetic ordering, for which the order parameter has symmetry $\mathrm{m}\Gamma_5^+$. This gives $\mathrm{m}\Gamma_2^+$, $\mathrm{m}\Gamma_4^+$ and $\mathrm{m}\Gamma_6^+$ as secondary order parameters but, as discussed in more detail by Haines *et al* (2019a) [42] and Haines *et al* (2019b) [43], moments allowed by $\mathrm{m}\Gamma_2^+$ and $\mathrm{m}\Gamma_6^+$ are not observed, implying that they are zero for reasons of thermodynamic stability. In combination, $\mathrm{m}\Gamma_4^+$ and $\mathrm{m}\Gamma_5^+$ give the observed magnetic structure in which there are ferromagnetic moments within Fe layers and antiferromagnetic moments between them, with freedom for the direction to rotate between $[100]^*$ and $[001]^*$. The change in order parameter which drives

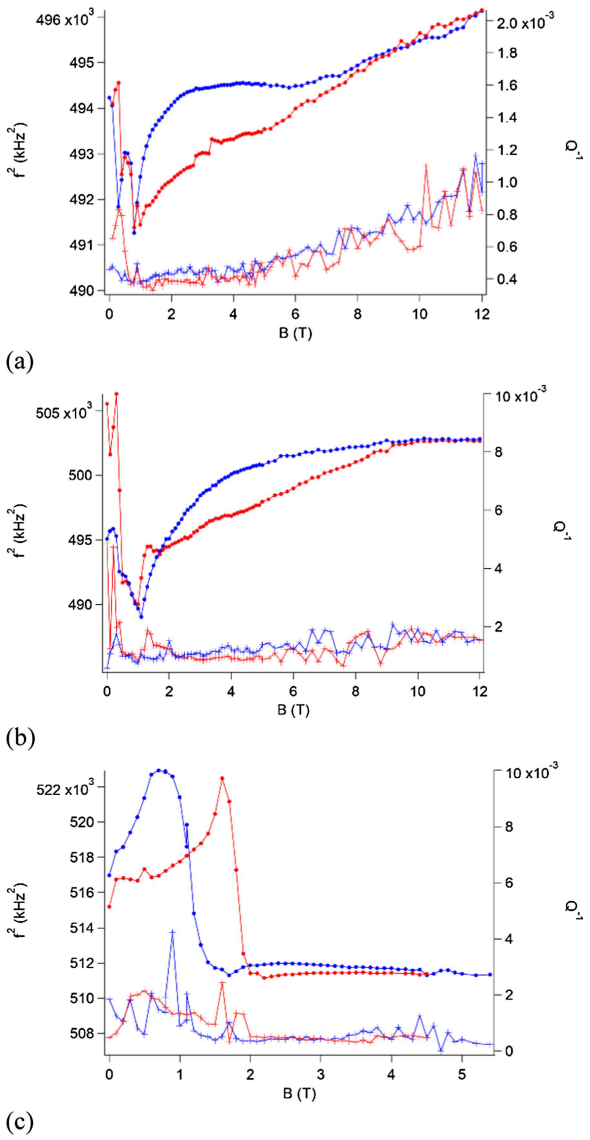

Figure 8. Variations of f^2 and Q^{-1} for resonance with $f \sim 700$ kHz at room temperature collected as a function of increasing (red) and decreasing (blue) field with $H//[\bar{1}20]^*$. (a) 60 K (b) 40 K (c) 20 K. Steep anomalies near 1 T at 60 K (and 40 K) are taken to indicate that a metamagnetic transition occurred. Applying a magnetic field perpendicular to the (001) plane was problematic as the sample was prone to be pushed out from between the transducers. Some data were recorded and are presented in appendix A2.

the C2′/c′ → P$\bar{1}$ transition is mΓ_5^+ $(-a,0.577a) \rightarrow$ mΓ_5^+ (a,b), allowing rotation of the moments out of the a–c plane.

5.2. Strain coupling

For kinetic reasons, it is unlikely that changes in vacancy ordering can occur at these low temperatures so that observed variations in spontaneous strain will be due to coupling only with the magnetic order parameters. By itself the proposed order parameter sequence mΓ_5^+ $(0,0) \rightarrow$ mΓ_5^+ $(0,a) \rightarrow$ mΓ_5^+ (a,b) would give $P6_3/mmc \rightarrow Cm'c'm \rightarrow P2_1/m$. From the full Landau expansion given in Haines *et al* (2019a) [42], the symmetry-breaking strain at the first transition is $(e_1–e_2)$ and at the second it is e_6. Both couple to the relevant order parameter components, q, with the form $\lambda e q^2$. The structure is already monoclinic due to shear strain e_4 ($\approx\cos\beta^*$ in the setting used by Haines *et al* 2020a [43]) arising from Fe/vacancy ordering, which means that the symmetry-breaking strain e_6 causes the Besnus transition to be monoclinic → triclinic rather than orthorhombic → monoclinic.

High resolution lattice parameter data of Koulialias *et al* (2018c) [30] from powder neutron diffraction obtained using a natural 4C sample did not reveal any measurable distortion from monoclinic lattice geometry but revealed small changes in the a- and b-parameters that are clearly related to the transition. Because of the non-linear contribution of saturation effects to thermal expansion as $T \rightarrow 0$ K, it is not possible to extract reliable values of linear strains but it is still possible to follow variations of cos β^*, where β^* is the reciprocal lattice angle of the $F2/d$ cell, and $(e_1–e_2)$. The latter can be estimated without significant loss of precision as $(a - b)/((ab)^{1/2})$. The temperature dependences of these two shear strains are shown in figure 9 and are consistent with variations over a wider temperature interval from the lattice parameter data of Powell *et al* (2004) [28] for a synthetic sample. The shear strain represented by cos β^* arises primarily from coupling with Fe/vacancy ordering (e_4 in the setting of Haines *et al* 2019 [43]). Variations below 300 K are presumably due to a weaker, additional contribution of coupling with the magnetic order parameter but there are no obvious changes associated specifically with the Besnus transition. In comparison, values of $(e_1 - e_2)$ are small at all temperatures and arise by weak coupling with the magnetic order parameter. They also show a distinct reduction below T_B from ∼0.002 to ∼0.001 (figure 9), confirming that the magnetic order parameter for the Besnus transition also couples with shear strain. An equivalent coupling of $e_6 \leqslant \sim 0.001$, would imply distortion of one of the monoclinic lattice angles from 90° to $\leqslant$ ∼90.06° and it is not surprising that such a small change has not yet been detected.

Weak coupling between shear strains and the magnetic order parameter is consistent with the very slight overall differences in shear elastic constants below and above T_B, as represented by changes in values of f^2 amounting to only ∼2–6% (figure 7). The fact that the net response is stiffening rather than softening is likely to be due to the time scale of relaxation of the magnetic order parameter. If the order parameter relaxes on the time scale of an induced strain, ie $\sim 10^{-5}$–10^{-6} s in an RUS experiment, coupling terms of the form $\lambda e q^2$ are expected to lead to softening. If the relaxation is slower than this, changes in the elastic constants are expected scale with q^2 due to higher order coupling terms with the form $\lambda e^2 q^2$. Stiffening occurs when the coupling coefficient, λ, is positive (e.g. references [54–56]).

If the Besnus transition occurs as a consequence of an electronic instability, such as a cooperative Jahn–Teller distortion for example, a separate driving order parameter, q_E, would be needed to describe the change from monoclinic to triclinic symmetry. This would belong to a zone centre irrep and would have bilinear coupling with the symmetry breaking shear strain, e_{sb}, as $\lambda e_{sb} q_E$ (Haines *et al* 2019 [42]). This, in

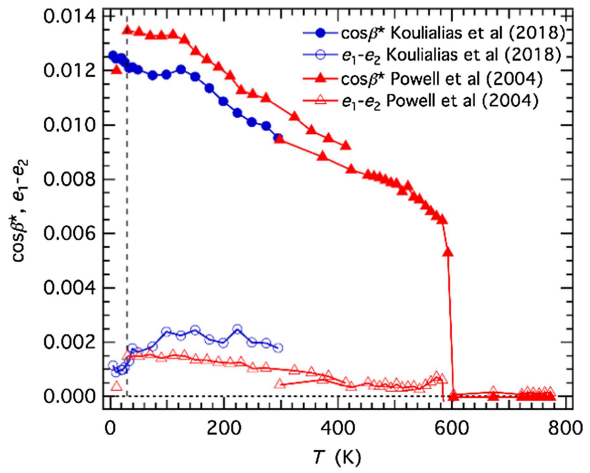

Figure 9. Variations of shear strains as a function of temperature for crystals with compositions near Fe_7S_8, determined from the lattice parameter data of Powell *et al* (2004) [28] for a synthetic sample and of Koulialias *et al* (2018 J. Phys. Condens. Matter **30** 425803) for a natural sample. (The two data sets of Powell *et al* were from different diffractometers). Large values of cos β^* arise primarily from coupling with the order parameter for Fe/vacancy ordering (Haines *et al* 2020a [43]). (Note: the reversal of sign for $(e_1 - e_2)$ in comparison with the values given by Haines *et al* (2019b) [43] is due to a different choice of setting of the unit cell with respect to the orthogonal reference axes).

turn, would give rise to non-linear softening of the related shear elastic constant as T_B is approached from above and below, characteristic of pseudoproper ferroelastic behaviour. Such a pattern of softening is not observed and it follows that, if there is an electronic component in the transition, it is a secondary effect. The observed elastic softening in a temperature interval of ∼5–10 K on either side of T_B is invariably accompanied by increased attenuation (figures 6 and 7(a) and (b)), signifying that it has a dynamical origin rather than being due to relaxation accompanying classical bilinear or linear/quadratic strain coupling.

5.3. Splitting of the Besnus transition

The transition at T_B is thermodynamically continuous [21] and has a physical origin that is likely to be essentially the same as for the spin–flop transition in end-member FeS and in crystals with other compositions in the $Fe_{1-x}S$ solid solution (Haines *et al* 2019 [42]). In general, for a purely magnetic transition due only to ordering of spins, the total entropy change is expected to be nR ln$(2s + 1)$ per mole, where the number of spin states, s, is 2 for Fe^{2+}, R is the gas constant and $n = 7$ for heat capacities expressed with respect to one mole of Fe_7S_8. This gives –93.6 J mol^{-1} K as the total magnetic entropy difference expected between fully disordered and fully ordered states. Above T_B there is already a high degree of magnetic order, however, and it is no surprise that the observed entropy change is only a fraction of this figure. If, as proposed by Wolfers *et al* (2011) [29] and Oddou *et al* (1992) [22], the transition is characterised by the breaking of symmetry specifically associated with the vacant cation site, the total entropy change might be nR ln2. Here $n = 1$ for the number of vacancy sites per mole and a degeneracy of 2 is attributed to ordering which relates simply to a doubling of the number of independent Fe cations in the structure. This gives $\Delta S = -5.76$ J mol^{-1} K, which, if there is also some electronic or phonon contribution, could reasonably account for the observed entropy change of ∼9 J mol^{-1} K from integration of the excess heat capacity (figure 1(b)).

[001]* is a magnetically hard direction of the 4C structure at room temperature and moments of the monoclinic structure only start to rotate substantially out of the basal plane below ∼250 K [28, 30]. Correlation of different properties measured on different pieces of the same original crystal show that rotation of the ferrimagnetic moment out of the a–c plane starts at ∼35 K, as measured in a field of 10 mT (figure 2(b)). Onset of the heat capacity anomaly in zero field is also at ∼35 K, but the maximum excess occurs at 32.9 K and there is a slight shoulder at ∼34.1 K (figure 1(a)). 35 K is also the temperature at which the steep reductions in both χ' and χ'' from AC magnetic data reach constant, low values (figure 5) and there is a second small peak at ∼32.5 K (figure 5(a)). A minimum in f^2 occurs between ∼33 and ∼36 K, and there is a peak in Q^{-1} near 32.5 K (figure 7(a)). The steepest variation in net magnetisation, given by the maximum value of dM dT^{-1}, probably occurs between ∼31 and ∼33 K (figure 2(c)). In detail, it thus appears that the transition is spread into two parts, with the onset of symmetry breaking due to changes in magnetic order occurring at ∼35 K and the main changes in thermodynamic properties, corresponding to the steepest change in the degree of order, occurring at ∼32.9 K. This difference is likely to be due to heterogeneity in the local magnetic structure arising from the presence of pre-existing ferrimagnetic domain walls.

Within magnetic domains of the $C2'/c'$ structure, the first magnetic order parameter, q_C, is large and within the walls it reduces to zero, with the possibility that coupling with the magnetic order parameter of the P$\bar{1}$ structure, q_P, could give rise to small variations in the value of the transition temperature. Biquadratic coupling of the form $\lambda q_C^2 q_P^2$ is expected for two transitions arising from different instabilities. For transition temperatures which are widely separated, the simplest solution for the Besnus transition has q_C remaining effectively constant, giving rise to the temperature dependent term of a conventional Landau expansion as $\frac{1}{2}a(T - T_B + \frac{2\lambda}{a}q_C^2)q_P^2$. In other words, the transition temperature for the second order transition is renormalised from T_B to $T_B - \frac{2\lambda}{a}q_C^2$. The peak in heat capacity would come from the domains, which form the bulk of the crystal and have $q_C \approx 1$, but a small positive value of λ would cause the onset of the magnetic transition to occur at a slightly higher temperature in the middle of the domain walls where $q_C = 0$.

The transfer of excess entropy from the main peak at 32.9 K to additional peaks at ∼34 and ∼35 K with increasing field up to 9 T (figure 1(b)) is most likely to be due to different parts of the crystal having slightly different transition temperatures depending on the orientation of the field with respect to the $C2'/c'$ structure. Volk *et al* (2018) [21] showed that T_B, as defined by the maximum of the temperature derivative of measured magnetisation, varies systematically between

~32 and ~34 K depending on the orientation of the field within the (001) plane. Their data for χ' and χ'' also suggest a difference of ~0.5 K between transition temperatures measured in directions parallel and perpendicular to (001). Three distinct transition points would be consistent with the presence of ferroelastic domains with three distinct crystallographic orientations, with respect to the orientation of the applied field, in the crystal used for the present study. Splitting of the transition in this way is consistent with the differences in excess entropy between different field strengths occurring only in the close vicinity of the transition point (figure 1(b)). The integrated excess entropy is the same, irrespective of field strength, once the transition has occurred in all parts of the crystal.

5.4. Ferroelastic and magnetic domains

Previous reports of domain configurations in natural pyrrhotite grains using the Bitter technique and the Magneto-optical Kerr effect have shown a characteristic pattern of lamellar 180° domains on a scale of ~2–30 μm [57–59]. Although not specified, the polarity of these domains is presumably parallel and antiparallel to the orientation of the individual moments determined by neutron diffraction, with domain walls close to (001) at room temperature. The observed values of θ and φ at room temperature for the orientation of the net moment are consistent with the crystal used in the present study containing a preponderance of twin domains which have $\varphi = 60°$, $\theta \approx 84°$ and $\varphi = 60°$, $\theta \approx 96°$ (including the expected out of plane angle of 6° from Powell *et al* 2004 [28]). The observed rotation from $\theta \approx 90°$ to ~58° at T_B, with φ remaining more or less constant (figures 2(b) and 3), also fits with the individual moments rotating within the a–c plane as temperature is reduced.

An abrupt change of trend of the net moment from decreasing θ at approximately constant φ to increasing φ at more or less constant θ, such that $\varphi \approx 60°$ at 35 K and ~90° at 2 K, matches the analysis of Wolfers *et al* (2011) [29] in relation to how the easy magnetisation direction would switch below a monoclinic → triclinic transition point. In particular, six-fold symmetry for the easy direction of a twinned crystal above T_B would become fourfold due to the twins being further split into two equal proportions. Volk *et al* (2016) [38] also found a rotation of the easy magnetisation direction with respect to the a–b plane below T_B and the same change from six-fold to four-fold symmetry.

The reduction in net magnetisation below T_B under ZFC measuring conditions resulted from cancellation of components of moments which have opposing orientations within new sets of magnetic twins. Poling of these by cooling in a 5 T field parallel to $[001]^*$ led to a net magnetisation that was larger by a factor of ~3 at 2 K than the magnetisation acquired during cooling in zero field (figure 4(a)). On the basis of evidence in the hysteresis loops, poling in a 5 T field applied parallel to $[100]^*$ and $[\bar{1}20]^*$ should also have caused an increase in remanent moment, M_r. Instead, a significant reduction in the net moment was observed when measured in a field of 10 mT after switching the 5 T field off (figure 1(a)). Failure of the crystal to remain poled in these two directions implies that magnetic twin domains renucleated when the high field was removed. On heating back up to temperatures above T_B, the distribution of moments between the original domain orientations was restored, reflecting the fact that the underlying configuration of twins and antiphase domains due to cation/vacancy ordering has a strong influence on the configuration of magnetic domains.

Ferroelastic twinning due to the change in point group symmetry $6/mmm \rightarrow 2/m$ has been analysed in detail by Haines *et al* (2019b) [43]. Most of the twin walls arising from vacancy ordering will be aligned nearly parallel to $[001]^*$, though there can also be one set aligned parallel to (001). A few individual twin walls were observed in the sample used in the present study by electron backscatter diffraction. The increase in c-dimension by a factor of 4 must result also in the development of antiphase domains with boundaries that can be non-conservative, in the sense that segments which are oriented parallel to (001) can have a local change in Fe:S ratio [60]. Reorientation of twin walls and non-conservative antiphase boundaries (APB's) from the configurations they acquired during slow cooling in nature requires Fe/vacancy diffusion. On the basis of the kinetic data of Herbert *et al* (2015) [35] discussed above, this is unlikely to occur to any significant extent during cycling below room temperature. Differences between ZFC and FC magnetisation in figure 2(a) show that an external field can induce rotation of the magnetic domains below T_B but that they return to their original configuration in the stability field of the monoclinic structure. Changes in the configuration of ferroelastic domains would cause changes in the elastic constants, as signified by changes in resonance frequencies of the RUS sample but, while there are changes between values measured before and after cooling through the Besnus transition (figures 7(a) and (c)), these are very small.

The orientation of new ferroelastic twin walls below the monoclinic $(2/m) \rightarrow$ triclinic $(\bar{1})$ transition will be the same as set out for the same change in point group symmetry in the mineral albite ($NaAlSi_3O_8$) by Salje (1993) [61] (and see, also Carpenter and Salje 1998 [56]). One set of twin walls will be parallel to (010) of the monoclinic structure and the second set perpendicular to this, with an orientation between the x- and z-axes that depends on the relative values of the triclinic shear strains (e_5 and e_6 for the setting in which e_4 is the strain associated with $\beta \neq 90°$ in the monoclinic structure). Evidence from conventional diffraction measurements is that any distortion from monoclinic lattice geometry below 35 K is small, however, and, hence, that strain contrast across the twin walls would be very small. It is unlikely that there will be any associated changes in Fe/vacancy distribution at these low temperatures, so that the twin walls should be free to change orientation in the same manner as the new magnetic domains when an external magnetic field is applied and they should not have the same memory effect as seen for ferroelastic domains arising from the hexagonal → monoclinic transition. It is not clear why resistance to reconfiguration of magnetic domains should be greatest when poling is induced parallel to $[001]^*$ at temperatures below T_B but the local strain heterogeneity of

ferroelastic twin walls of the monoclinic structure and local chemical heterogeneity of non-conservative APB's could act as effective sites for re-nucleation of magnetic domains to cause depoling in the other two directions.

5.5. Metamagnetic transitions

Evidence for a metamagnetic transition is seen in the magnetic hysteresis loops measured with $H//[\bar{1}20]^*$ (figure 4(c)), and there are changes in elastic properties at 60 and 40 K with a pattern of softening/stiffening and acoustic loss (figures 8(a) and (b)) which is closely similar to the pattern associated with the Besnus transition observed with varying temperature in zero field. The new magnetic structure at high fields has not been characterised but is most likely to involve some different combination of non-zero components of the mΓ irreps. The M–H loop measured with $H//[\bar{1}20]^*$ at 20 K does not show evidence of a metamagnetic transition, but there are hysteretic changes in elastic properties at ∼1 T (figure 8(c)) which are quite different from those associated with the Besnus transition. It remains to be seen whether the elastic anomaly is due to a first order metamagnetic transition or to a change in the configuration of ferroelastic twin domains, but it appears that the H–T phase diagram would have an interesting topology.

5.6. Dynamics: AC magnetic and acoustic loss

The principal features of the χ'' variations reported here (figure 5) are closely similar to those reported previously [21, 32, 36]. In particular, the temperature at which the peak occurs immediately above T_B is independent of measuring frequency, indicating that it is not due to a thermally activated loss process [36]. The steep reduction to more or less constant values below T_B has been attributed to a reduction of the mobility of 180° magnetic domain walls by additional pinning effects in the stability field of the low temperature structure [32]. A small peak observed a few degrees below the steep reduction coincides with the peak in heat capacity measured in zero field (Volk *et al* 2018 [21] and compare figures 1(a) and 5(a) above). This association must be due to some aspect of changing dynamics of local moments at the temperature(s) where the temperature dependence of the new magnetisation is at a maximum. The weak anomaly is present when the measuring field is applied in a direction within the plane (001) but not when the direction is perpendicular to (001), presumably depending on the orientation of new domain walls in the low temperature structure.

Variations of Q^{-1} shown in figure 8 have a different overall form in comparison with those of χ''. Acoustic loss is relatively high in the stability field of the monoclinic structure but reduces with falling temperature (figure 8). Because ferroelastic twin walls generated at the hexagonal → monoclinic transition are tied to Fe/vacancy ordering, it is unlikely that the loss mechanism is due to their displacement under the low stress conditions and short timescales of a natural acoustic resonance. The loss mechanism is presumably due to motion of unspecified defects which couple locally with strain, including local variations in spin state and magnetoelastic coupling.

The onset of softening ahead of T_B occurs at ∼45 K and has a pattern typical of fluctuations of an order parameter with coupling to strain ahead of a co-elastic or improper ferroelastic phase transitions, such as occurs in quartz and perovskites for example [62, 63]. The transition itself is then marked by an interval of increased acoustic loss (high values of Q^{-1}) which coincides with a small amount of elastic softening followed by stiffening (figures 6 and 7). A minimum in f^2 occurs between ∼33 and ∼36 K, but the variations of Q^{-1} become hard to follow in this interval because of the broadness of the primary resonance peaks. The most reliable measurements of peak width appear to indicate that there is a maximum in Q^{-1} between ∼32 and ∼32.5 K, which coincides with the peak in heat capacity (figure 1(a)) and the small, rounded peak in χ'' (figure 5(a)). In principle, the mobility of the second generation of ferroelastic twin walls discussed above would be expected to be restricted at such low temperatures. However, the thickness, w, of ferroelastic twin walls varies as $w \propto (T_c - T)^{-1}$ below a second order transition [64–66] and thick twins are less likely to be pinned by defects that thin ones. This means that there can be a narrow temperature interval immediately below the transition point where more or less well developed but thick twin walls develop and would be mobile under the influence of an external stress field. It is tentatively proposed, therefore, that the anomalies in Q^{-1} and χ'' reflect dynamical magnetoelastic coupling related to fluctuations of the magnetic order parameter above T_B and to new twin walls immediately below T_B. The mobility of the ferroelastic twin walls then diminishes steeply due to pinning when they become thinner as T reduces away from T_B.

Splitting of the Besnus transition into two parts in figure 7(d), with minima in f^2 at ∼34.5 and ∼37.5 K, and peaks in Q^{-1} at slightly lower temperatures, might be taken to indicate that there are two discrete phase transitions in a 9 T field with $H//[\bar{1}20]^*$, but it is more likely that they represent transitions in two twin domains with different orientations with respect to the applied field.

6. Conclusions

(a) Variations of the thermodynamic, magnetic and elastic properties through the Besnus transition at ∼33 K in a natural sample of 4C pyrrhotite with composition close to Fe_7S_8 have been tested against the group theoretical model of Haines *et al* (2019a) [42] for coupling between order parameters relating to Fe/vacancy ordering (irrep $U_1(1/2,0,1/4)$) and magnetic ordering (irreps $m\Gamma_4^+$ and $m\Gamma_5^+$).

(b) The physical origin of the transition can be understood as being related to the spin–flop transition at ∼450 K in FeS, modified by the presence of vacancies and the influence of the Fe/vacancy ordering scheme. No evidence has been found for an additional electronic instability.

(c) It is unlikely, for kinetic reasons, that changes in Fe/vacancy ordering occur through the transition point but details of the transition appear to be controlled by the pre-existing microstructure due to the $P6_3/mmc \rightarrow C2'/c'$

transition which occurs during slow cooling in nature. In particular, an unusual splitting of the transition could be understood in terms of differences in magnetic structure between the pre-existing magnetic domain walls and the domains that they separate.

(d) The proposed change in symmetry, $C2'/c' \rightarrow P\bar{1}$, will necessarily result in the development of a new set of ferroelastic twin walls but coupling of the magnetic order parameter with the symmetry-breaking strain is weak and the only evidence for these is a peak in the acoustic loss at a temperature which correlates with a small peak in the imaginary component of the AC susceptibility.

(e) Changes in the elastic properties are consistent with weak magnetoelastic coupling and relaxation times of the magnetic order parameter, in response to an applied stress, that are longer than $\sim 10^{-5}$–10^{-6} s.

(f) Evidence for metamagnetic transitions under the influence of a field applied to $[\bar{1}20]^*$ suggests that H–T phase diagrams should display an interesting diversity of magnetic structures. The stability of these will depend on coupling with the underlying Fe/vacancy ordering, for which a common strain coupling mechanism is likely to be important.

Acknowledgments

This work was funded by a grant from the Leverhulme Foundation (RPG-2016-298), which is gratefully acknowledged. RUS facilities have been established and maintained in Cambridge through grants from the Natural Environment Research Council and the Engineering and Physical Sciences Research Council of Great Britain to MAC (NE/B505738/1, NE/F17081/1, EP/I036079/1). Heat capacity, DC and AC magnetisation measurements were carried out using the Advanced Materials Characterisation Suite, funded by EPSRC Strategic Equipment Grant EP1M00052411.

Appendix A

A1. Heat capacity entropy calculation

To obtain a reliable estimate of the excess entropy associated with the Besnus transition it is necessary to define a baseline heat capacity. This is not always easy and often the method of defining the baseline can have serious implications for the extracted entropy. Following the standard procedure of fitting a polynomial to the data above and below temperatures semi-arbitrarily deemed to be 'far away' from the transition gave approximate results. However, the order of the polynomial and the exact cut off temperatures used had a reasonably significant effect on the extracted excess entropy. Fortunately, in this case, an independent baseline could be defined from the heat capacity of a very similar pyrrhotite sample in which the Besnus transition does not occur. The measurement used was of a piece of 5C pyrrhotite that had been cut from the same crystal as the 4C sample studied here. The curve from the 5C sample was scaled to that of the sample used here with a single scale factor that matched the values of the two curves over the range 220–270 K. This eliminates the error from the mass measurements of the two samples. The baseline that is removed from the 4C data to extract the excess entropy was a 5th order polynomial fit of the scaled 5C heat capacity in the temperature range 2–60 K. The coefficients of the fit are: $M_0 = 1.0823$, $M_1 = -3.3234 \times 10^{-1}$, $M_2 = 2.1183 \times 10^{-2}$, $M_3 = 2.0110 \times 10^{-3}$, $M_4 = -4.6962 \times 10^{-5}$ and $M_5 = 2.9878 \times 10^{-7}$, where M_i are the coefficients of the ith order term.

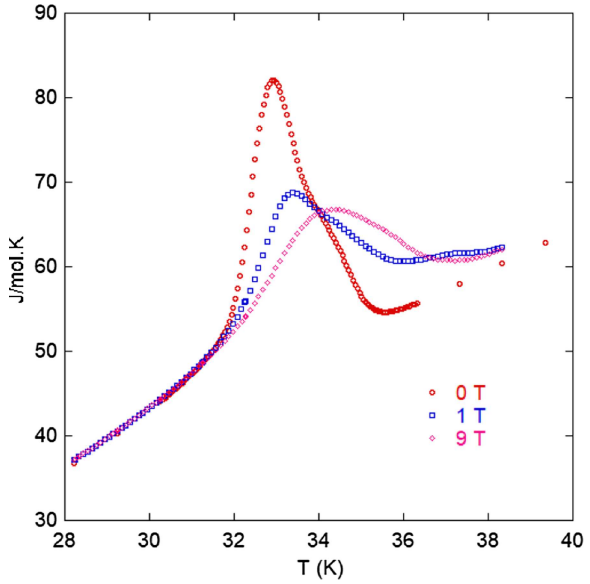

Figure A1. Heat capacity of crystal 1 with the field applied perpendicular to the (001) plane.

A2. Measurements with the field applied perpendicular to the (001) plane

Measurements of heat capacity and RUS were also made with an external magnetic field applied in the direction normal to the (001) plane. When the field was applied perpendicular to the (001) plane, the peak in the heat capacity associated with the Besnus transition was not split into two or three peaks, as seen in the data presented in figure 1 with the field applied within the (001) plane, but is pushed to higher temperatures and broadened considerably (see figure A1). The high field data were scaled to match the zero-field data over the range 60–180 K. There are no significant features in this range. The scaling is necessary due to a slight discrepancy in the addenda measurements over the two separate runs. RUS data with a field of 2 T perpendicular to the (001) plane were also measured. The resulting variations of f^2 and Q^{-1} are shown in figure A2.

A3. RUS Data for the Volk et al Sample

Variations of f^2 and Q^{-1} from RUS spectra of a crystal from the sample described by Volk *et al* 2016 and 2018. [21, 38] are shown in figure A3. There is no measureable hysteresis between spectra measured on cooling (blue) and heating (red) (figure A3(a)). The average temperature of the minimum in

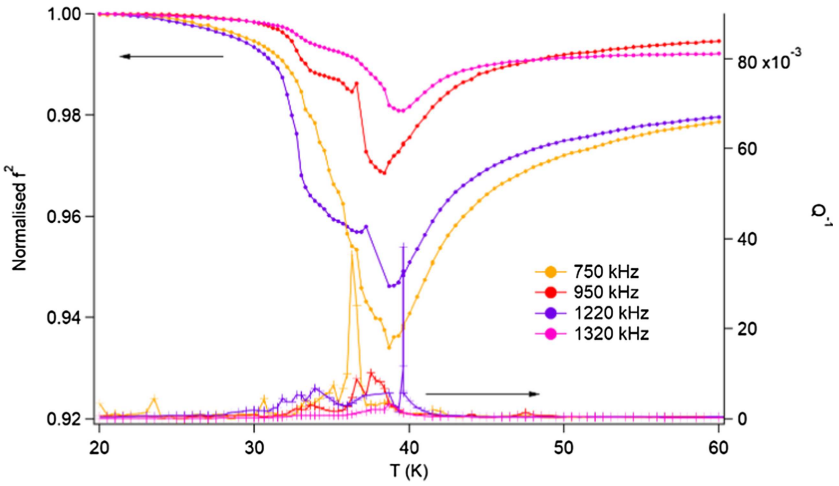

Figure A2. Results of peak fitting of RUS spectra collected from crystal 1 with a magnetic field of 2 T applied in a direction perpendicular to (001).

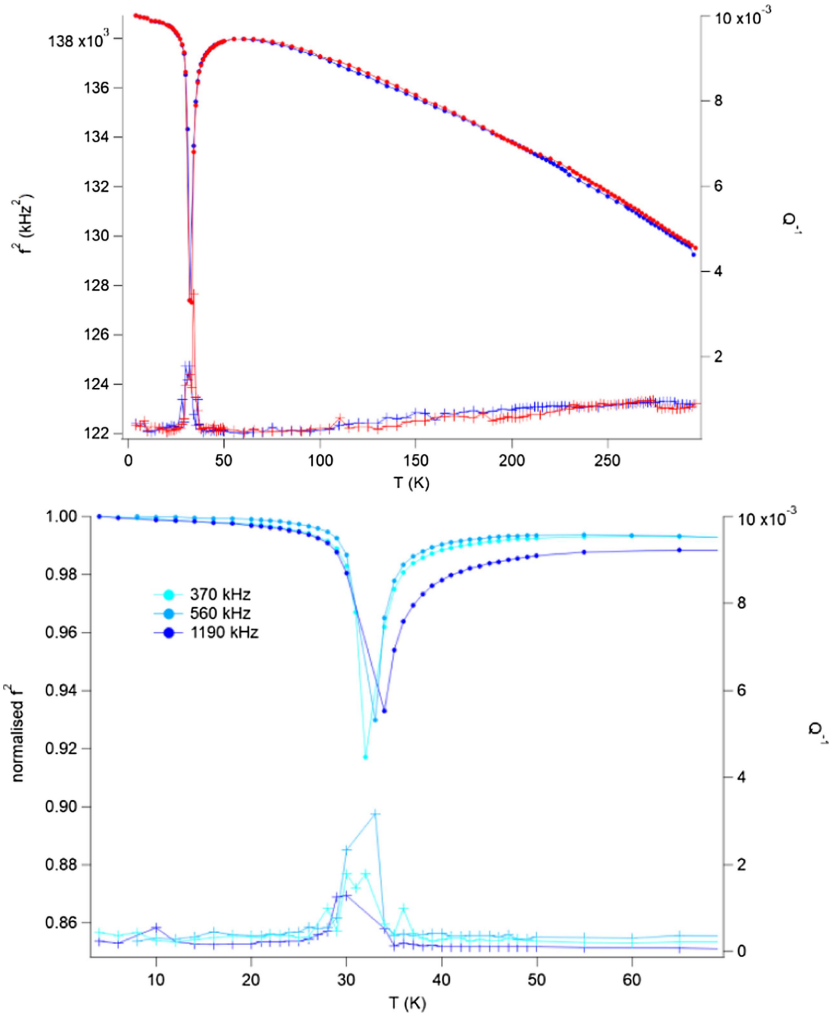

Figure A3. Variations of f^2 and Q^{-1} for the sample characterised by Volk *et al* 2016 and 2018 [21, 38].

f^2 for three peaks around the Besnus transition is 33 ± 1 K (figure A3(b)).

ORCID iDs

C R S Haines https://orcid.org/0000-0002-1274-8329
M A Carpenter https://orcid.org/0000-0003-2855-0007

References

[1] Morrish A H 1994 *Canted Antiferromagnetism: Hematite* (Singapore: World Scientific)
[2] Jackson M, Bowles J and Moskowitz B 2011 Interpretation of low-temperature data part III: the magnetite Verwey transition (part A) *IRM Q.* **20** 7–11
[3] Senn M S, Wright J P and Attfield J P 2012 Charge order and three-site distortions in the Verwey structure of magnetite *Nature* **481** 173–6
[4] Harrison R J 2009 Magnetic ordering in the ilmenite-hematite solid solution: a computational study of the low-temperature spin glass region *Geochem., Geophys., Geosyst.* **10** 1–17
[5] Yamanaka T, Mine T, Asogawa S and Nakamoto Y 2009 Jahn–Teller transition of Fe_2TiO_4 observed by maximum entropy method at high pressure and low temperature *Phys. Rev.* B **80** 134120
[6] Rochette P 1987 Metamorphic control of the magnetic mineralogy of black shales in the Swiss Alps: toward the use of magnetic isograds *Earth Planet. Sci. Lett.* **84** 446–56
[7] Pucher R 1994 Pyrrhotite-induced aeromagnetic anomalies in western Germany *J. Appl. Geophys.* **32** 33–42
[8] Rochette P, Fillion G, Mattéi J-L and Dekkers M J 1990 Magnetic transition at 30-34 Kelvin in pyrrhotite: insight into a widespread occurrence of this mineral in rocks *Earth Planet. Sci. Lett.* **98** 319–28
[9] Rochette P, Lorand J-P, Fillion G and Sautter V 2001 Pyrrhotite and the remanent magnetization of SNC meteorites: a changing perspective on Martian magnetism *Earth Planet. Sci. Lett.* **190** 1–12
[10] Rochette P, Gattacceca J, Chevrier V, Hoffmann V, Lorand J-P, Funaki M and Hochleitner R 2005 Matching Martian crustal magnetization and magnetic properties of Martian meteorites *Meteorit. Planet. Sci.* **40** 529–40
[11] Andresen A F, Torbo P, Ostlund E, Bloom G and Hagen G 1967 Phase transitions in Fe_xS ($x = 0.90$–1.00) studied by neutron diffraction *Acta Chem. Scand.* **21** 2841–8
[12] Schwarz E J and Vaughan D J 1972 Magnetic Phase Relations of Pyrrhotite *J. Geomagn. Geoelectr.* **24** 441–58
[13] Bennett C E G and Graham J 1980 New observations on natural pyrrhotites. Part III. Thermomagnetic experiments *Am. Mineral.* **65** 800
[14] Grønvold F and Stølen S 1992 Thermodynamics of iron sulfides II. Heat capacity and thermodynamic properties of FeS and of $Fe_{0.875}S$ at temperatures from 298.15 K to 1000 K, of $Fe_{0.98}S$ from 298.15 K to 800 K, and of $Fe_{0.89}S$ from 298.15 K to about 650 K. Thermodynamics of formation *J. Chem. Thermodyn.* **24** 913–36
[15] Wang H and Salveson I 2005 A review on the mineral chemistry of the non-stoichiometric iron sulphide, $Fe_{1-x}S$ ($0 \leqslant x \leqslant 0.125$): polymorphs, phase relations and transitions, electronic and magnetic structures *Phase Transit.* **78** 547–67
[16] Pearce C I, Pattrick R and Vaughan D J 2006 Electrical and magnetic properties of sulfides *Rev. Mineral. Geochem.* **61** 127–180
[17] Besnus M J and Meyer A J P 1964 Nouvelles donnees experimentales sur lemagnetisme de la pyrrhotine naturelle *Proc. Int. Conf. Mag. Nottingham 1964* 507–11
[18] Rochette P, Fillion G and Dekkers M J 2011 Interpretation of low-temperature data part 4: the low-temperature magnetic transition of monoclinic pyrrhotite *Inst. Rock Magn.* **21** 1
[19] Fillion G and Rochette P 1988 The low temperature transition in monoclinic pyrrhotite *J. Phys. Colloq.* **49** C8–907
[20] Dunlop D J 2015 Transition warming and cooling remanences in pyrrhotite and hematite *Geophys. J. Int.* **203** 605–13
[21] Volk M W R, McCalla E, Voigt B, Manno M, Leighton C and Feinberg J M 2018 Changes in physical properties of 4C pyrrhotite (Fe_7S_8) across the 32 K Besnus transition *Am. Mineral.* **103** 1674–89
[22] Oddou J L, Jeandey C, Mattei J L and Fillion G 1992 Mössbauer study of the low-temperature transition in pyrrhotite *J. Magn. Magn. Mater.* **104–107** 1987–8
[23] Grønvold F, Westrum E F and Chou C 1959 Heat capacities and thermodynamic properties of the pyrrhotites FeS and $Fe_{0.877}S$ from 5 to 350 K *J. Chem. Phys.* **30** 528–31
[24] Dekkers M J, Mattéi J-L, Fillion G and Rochette P 1989 Grain-size dependence of the magnetic behavior of pyrrhotite during its low-temperature transition at 34 K *Geophys. Res. Lett.* **16** 855–8
[25] Jeandey C, Oddou J L, Mattei J L and Fillion G 1991 Mössbauer investigation of the pyrrhotite at low temperature *Solid State Commun.* **78** 195–8
[26] Li F and Franzen H F 1996 Ordering, incommensuration, and phase transitions in pyrrhotite: part II: a high-temperature x-ray powder diffraction and thermomagnetic study *J. Solid State Chem.* **126** 108–20
[27] Fillion G, Mattei J L, Rochette P and Wolfers P 1992 Neutron study of 4C pyrrhotite *J. Magn. Magn. Mater.* **104–107** 1985–6
[28] Powell A V, Vaqueiro P, Knight K S, Chapon L C and Sanchez R D 2004 Structure and magnetism in synthetic pyrrhotite Fe_7S_8: a powder neutron-diffraction study *Phys. Rev.* B **70** 014415
[29] Wolfers P, Fillion G, Ouladdiaf B, Ballou R and Rochette P 2011 The pyrrhotite 32 K magnetic transition *Solid State Phenom.* **170** 174–9
[30] Koulialias D, Canévet E, Charilaou M, Weidler P G, Löffler J F and Gehring A U 2018 The relation between local structural distortion and the low-temperature magnetic anomaly in Fe_7S_8 *J. Phys.: Condens. Matter* **30** 425803
[31] Armstrong J N, Hua S Z and Chopra H D 2013 Anisotropic Curie temperature materials *Phys. Status Solidi* **250** 387–95
[32] Kind J, García-Rubio I, Charilaou M, Nowaczyk N R, Löffler J F and Gehring A U 2013 Domain-wall dynamics in 4*C* pyrrhotite at low temperature *Geophys. J. Int.* **195** 192–9
[33] Feinberg J M, Solheid P A, Swanson-Hysell N L, Jackson M J and Bowles J A 2015 Full vector low-temperature magnetic measurements of geologic materials *Geochem., Geophys., Geosyst.* **16** 301–14
[34] Charilaou M, Kind J, Koulialias D, Weidler P G, Mensing C, Löffler J F and Gehring A U 2015 Magneto-electronic coupling in modulated defect-structures of natural $Fe_{1-x}S$ *J. Appl. Phys.* **118** 83903
[35] Herbert F W, Krishnamoorthy A, Yildiz B and Van Vliet K J 2015 Diffusion-limited kinetics of the antiferromagnetic to ferrimagnetic λ -transition in $Fe_{1-x}S$ *Appl. Phys. Lett.* **106** 2–7
[36] Koulialias D, Kind J, Charilaou M, Weidler P G, Löffler J F and Gehring A U 2016 Variable defect structures cause the magnetic low-temperature transition in natural monoclinic pyrrhotite *Geophys. J. Int.* **204** 961–7
[37] Bezaeva N S, Chareev D A, Rochette P, Kars M, Gattacceca J, Feinberg J M, Sadykov R A, Kuzina D M and Axenov S N 2016 Magnetic characterization of non-ideal single-domain monoclinic pyrrhotite and its demagnetization under hydrostatic pressure up to 2 GPa with implications for impact demagnetization *Phys. Earth Planet. Inter.* **257** 79–90

[38] Volk M W R, Gilder S A and Feinberg J M 2016 Low-temperature magnetic properties of monoclinic pyrrhotite with particular relevance to the Besnus transition *Geophys. J. Int.* **207** 1783–95
[39] Ferrow E, Adetunji J and Nkoma J S 2006 Characterization of pyrrhotite in Cu–Ni-ore bodies from mines in Botswana by Mössbauer spectroscopy, x-ray diffraction, and thermomagnetometry *Eur. J. Mineral.* **18** 653–64
[40] Koulialias D, Charilaou M, Schäublin R, Mensing C, Weidler P G, Löffler J F and Gehring A U 2018 Ordered defects in $Fe_{1-x}S$ generate additional magnetic anisotropy symmetries *J. Appl. Phys.* **123** 033902
[41] Koulialias D, Charilaou M, Mensing C, Löffler J F and Gehring A U 2018 Torque analysis of incoherent spin rotation in the presence of ordered defects *Appl. Phys. Lett.* **112** 1–5
[42] Haines C R S, Howard C J, Harrison R J and Carpenter M A 2019 Group-theoretical analysis of structural instability, vacancy ordering and magnetic transitions in the system troilite (FeS)–pyrrhotite ($Fe_{1-x}S$) *Acta Crystallogr.* B **75** 1208–24
[43] Haines C R S, Lampronti G I and Carpenter M A 2020 Magnetoelastic coupling associated with vacancy ordering and ferrimagnetism in natural pyrrhottie, Fe7S8 (in preparation)
[44] Li G and Gladden J R 2010 High temperature resonant ultrasound spectroscopy: a review *Int. J. Spectrosc.* **2010** 206362
[45] Migliori A, Sarrao J L, Visscher W M, Bell T M, Lei M, Fisk Z and Leisure R G 1993 Resonant ultrasound spectroscopic techniques for measurement of the elastic moduli of solids *Physica* B **183** 1–24
[46] Migliori A and Maynard J D 2005 Implementation of a modern resonant ultrasound spectroscopy system for the measurement of the elastic moduli of small solid specimens *Rev. Sci. Instrum.* **76** 121301
[47] Zadler B J, Le Rousseau J H L, Scales J A and Smith M L 2004 Resonant ultrasound spectroscopy: theory and application *Geophys. J. Int.* **156** 154–69
[48] Maynard J 1996 Resonant ultrasound spectroscopy *Phys. Today* **49** 26
[49] McKnight R E A, Carpenter M A, Darling T W, Buckley A and Taylor P A 2007 Acoustic dissipation associated with phase transitions in lawsonite, $CaAl_2Si_2O_7(OH)_2{\cdot}H_2O$ *Am. Mineral.* **92** 1665–72
[50] Schiemer J, Spalek L J, Saxena S S, Panagopoulos C, Katsufuji T, Bussmann-Holder A, Köhler J and Carpenter M A 2016 Magnetic field and *in situ* stress dependence of elastic behavior in $EuTiO_3$ from resonant ultrasound spectroscopy *Phys. Rev.* B **93** 54108
[51] Evans D M, Schiemer J A, Schmidt M, Wilhelm H and Carpenter M A 2017 Defect dynamics and strain coupling to magnetization in the cubic helimagnet Cu_2OSeO_3 *Phys. Rev.* B **95** 1–11
[52] Haines C R S, Lampronti G I, Klooster W T, Coles S J, Dutton S E and Carpenter M A 2020b Morin-type transition in 5C pyrrhotite *Am. Mineral.* https://doi.org/10.2138/am-2020-7266
[53] Besnus M J, Munschy G and Meyer A J P 1968 Sublattice rotations in ferrimagnets: the case of pyrrhotite *J. Appl. Phys.* **39** 903–4
[54] Rehwald W 1973 The study of structural phase transitions by means of ultrasonic experiments *Adv. Phys.* **22** 721–55
[55] Lüthi B and Rehwald W 1981 *Ultrasonic Studies Near Structural Phase Transitions Structural Phase Transitions I* ed K A Müller and H Thomas (Berlin: Springer) pp 131–84
[56] Carpenter M A and Salje E K H 1998 Elastic anomalies in minerals due to structural phase transitions *Eur. J. Mineral.* **10** 693–812
[57] Soffel H C 1981 Domain structure of natural fine-grained pyrrhotite in a rock matrix (diabase) *Phys. Earth Planet. Inter.* **26** 98–106
[58] Soffel H C 1977 Pseudo-single-domain effects and single-domain multidomain transition in natural pyrrhotite deduced from domain-structure observations *J. Geophys.* **42** 351–9
[59] Appel E, Hoffmann V and Soffel H C 1990 Magneto-optical Kerr effect in (titano)magnetite, pyrrhotite and hematite *Phys. Earth Planet. Inter.* **65** 36–42
[60] Harries D, Pollok K and Langenhorst F 2011 Translation interface modulation in *NC*-pyrrhotites: direct imaging by TEM and a model toward understanding partially disordered structural states *Am. Mineral.* **96** 716–31
[61] Salje E K 1993 *Phase Transitions in Ferroelastic and Co-elastic Crystals* (Cambridge: Cambridge University Press)
[62] Carpenter M A, Salje E K H, Graeme-Barber A, Wruck B, Dove M T and Knight K S 1998 Calibration of excess thermodynamic properties and elastic constant variations associated with the $\alpha \leftrightarrow \beta$ phase transition in quartz *Am. Mineral.* **83** 2–22
[63] Carpenter M A 2015 Static and dynamic strain coupling behaviour of ferroic and multiferroic perovskites from resonant ultrasound spectroscopy *J. Phys.: Condens. Matter* **27** 263201
[64] Wenyuan S, Huiman S, Yuning W and Baosheng L 1985 Internal friction associated with domain walls and ferroelastic phase transition in Lnpp *Le J. Phys. Colloq.* **46** C10–609
[65] Yening W, Wenyuan S, Xiaohua C, Huimin S and Baosheng L 1987 Internal friction associated with the domain walls and the second-order ferroelastic transition in LNPP *Phys. Status Solidi* **102** 279–85
[66] Chrosch J and Salje E K H 1999 Temperature dependence of the domain wall width in $LaAlO_3$ *J. Appl. Phys.* **85** 722–7